Available online at www.sciencedirect.com
ScienceDirect
Computers & Fluids 37 (2008) 1011–1028
computers & fluids
www.elsevier.com/locate/compfluid

Multiple states, topology and bifurcations of natural convection in a cubical cavity

Tony W.H. Sheu [a,*], H.P. Rani [a], Teu-Chia Tan [a], S.F. Tsai [b]

[a] Department of Engineering Science and Ocean Engineering, National Taiwan University, Taipei 10617, Taiwan, ROC
[b] Department of Marine Engineering, National Taiwan Ocean University, Keelung, Taiwan, ROC

Received 30 May 2007; received in revised form 4 October 2007; accepted 27 November 2007
Available online 5 December 2007

Abstract

A numerical investigation has been conducted to explore the steady nonlinear low Prandtl number flow/thermal transition in a differentially heated cubic cavity. For small values of Rayleigh number (*Ra*), it is observed that initially there was only one symmetric steady-state solution. When the *Ra* was amplified, the system bifurcates from one fixed-point solution to the two stationary solutions, namely, Mode I and Mode II pitchfork bifurcations. This is due to the symmetric nature existing along the vertical and diagonal planes. The flow structure in the present nonlinear system consists of a pair of asymmetric counter-rotating helical cells in a double helix structure, foliated with invariant helically symmetric surfaces containing the fibre-like fluid particle orbits. Also the evolution of different symmetry-breaking orientations on the transverse and diagonal planes of the cavity was noticed. In the Mode I orientation a symmetric vortex coreline was observed. However, in the Mode II orientation a pair of anti-symmetric vortex corelines was observed. Detailed topological study was made based on the rule of Hunt and the structural stability criteria. Also the simulated results were corroborated with numerical evidence. The existence of the critical *Ra* values was ascertained with the aid of the predicted L_2-error norms, thermal/flow iso-contours and streamlines. The route of Mode I orientation was made of the alternate symmetric and asymmetric flows as *Ra* was augmented.

1. Introduction

In recent years, there has been a growing interest in studying the liquid metal flow in cavities subjected to an external temperature gradient. In the process of solidification of binary alloys and crystal growth in melt fluids, the thermal and concentration buoyancy forces can either aid (or oppose) each other depending on the type of alloy and the process of heating (or/and cooling). When the fluid is heated from below, the flow exhibits a very strong and complex nonlinear behavior which is of primary importance in the solar collector design, passive energy storage, crystal growth and in the micro-manufacturing techniques [1]. For example, in the electronic industry the solid/liquid interface is strongly affected by the heat convection [2]. Stable dynamic solutions of these convection problems are important for practical applications because of their impact on the control of dopant distribution. In the past several decades, the Rayleigh–Bérnard problem had been slightly modified so as to make this classical problem more closely related to the destabilized vertical Bridgman crystal growth system. Intensive theoretical, experimental and numerical studies have been done especially in the infinite horizontal layers and in the relatively shallow cavities.

McFadden and Coriell [3] and Impey et al. [4] have studied the two dimensional (2D) model of the directional solidification configuration for the solutal control. The same problem under the low gravity condition was analyzed by Alexander et al. [5]. The thermal control conditions were used by Larroude et al. [6] to investigate the

* Corresponding author. Tel.: +886 2 3366 5746; fax: +886 2 2392 9885.
E-mail address: twhsheu@ntu.edu.tw (T.W.H. Sheu).

0045-7930/$ - see front matter © 2007 Elsevier Ltd. All rights reserved.
doi:10.1016/j.compfluid.2007.11.003

2D Rayleigh–Bénard problem. Computational results presented in these papers were used to analyze the dynamic interaction with the solid/liquid transition. The three dimensional (3D) experimental studies of the problem of current interest have been reported by Bratsun et al. [7]. They showed that an initially symmetric cavity flow could become asymmetric as the Grashof number was increased beyond a critical value. Lan and Yang [8] addressed the oscillatory responses to pulse disturbances in the furnace of a 2D vertical zone-melting system and studied the symmetry-breaking steady-state flows in a simplified 3D vertical zone-melting system [9]. Such a symmetry-breaking phenomenon (or pitchfork bifurcation) in a symmetric physical domain is termed as the Coanda effect [10]. According to Bennacer et al. [11] this symmetry-breaking phenomenon has been influenced by the cavity height and the externally applied temperature gradient. Bifurcation in a nonlinear system is a qualitative change in the dynamics of that system. Bennacer et al. [11] also showed that the bifurcation type might change when a controlling parameter (Rayleigh number (Ra) in the current study) was varied. Transition to chaos is also shown to depend on the critical Rayleigh number. For this cavity problem, Davis [12] and Stork and Muller [13] have concluded that the critical Rayleigh number ($Ra = 1708$) was independent of the Prandtl number (Pr). Erenburg et al. [14] studied the solution multiplicity, stability and bifurcation of low Prandtl number steady natural convection in a two-dimensional rectangular cavity. They observed that laminar oscillatory flows exist around each unstable steady-state branch, which leads to a multiplicity of steady and oscillatory state. From the stability diagram they also observed the marginal stability curves corresponding to the steady symmetry-breaking bifurcations.

Recently 3D computations have been limited to high Pr and provided us a general understanding of the flow development [15,16]. Hence, it is important to analyze the inherent nonlinear transition from symmetric to asymmetric equilibrium states with the increased Ra at the low Prandtl number. For the hydrodynamic/thermal instability problems, the direct numerical simulation (DNS) of 3D time-dependent Navier–Stokes equations is extremely time-consuming. The commonly used linear theory can be applied only for the system state not far from equilibrium, *i.e.*, linear theory is appropriate only for the first bifurcation [17]. The experimental evidence of the nonlinear behaviors in a system and measurements of the significant data such as critical values of the governing parameters for the bifurcations are usually of considerable uncertainty and sometimes difficult to obtain. To explore the nonlinear dynamics including the bifurcation and the routes to chaos of the system we have focused our attention on the natural convection in a cubical cavity subjected to the low Pr based on the DNS results. Our aim is to provide a detailed nonlinear analysis of the symmetry-breaking thermal/flow fields in the investigated buoyancy driven cubical cavity. The major bifurcation type seen frequently in the nonlinear system is the pitchfork bifurcation, which is characterized by the appearance of symmetry-breaking solution. This pitchfork bifurcation can produce some unsteadiness in the flow and consequently perturb the solid/liquid interface and the dopant distribution. The onset of pitchfork bifurcation points in the parameter space is, thus, important to be identified.

The paper is organized as follows. The equations and the prescribed boundary conditions, the symmetries of the problem and their implications along with the theoretical details are summarized in Section 2. The subsequent Section 3 deals with the employed numerical methods along with the grid validation. In Section 4, the flow features are extracted and well represented in terms of topology, which is spanned by different kinds of critical points. The critical point analysis was also presented to show that the simulated velocity vector field satisfies the topological rule of Hunt [18] and the structural stability criteria. This is followed by providing the corroborative numerical evidence. Further, the multiple solutions and the symmetry-breaking (or pitchfork bifurcation) phenomenon were analyzed with the help of the iso-contours of heat flux and the flow variables in the wide range of Rayleigh numbers. The vortical nature was analyzed for the two possible solutions existing in the currently investigated nonlinear system. In addition, the global pitchfork bifurcation scenario for the critical parameter Ra was presented. The conclusions are drawn finally in Section 5.

2. Numerical model

The geometry of an axisymmetric cubical cavity (length $L = 1$ m) containing the liquid metal Tin (Sn) of low Pr (=0.01) is shown in Fig. 1. The Cartesian coordinate frame of reference (x, y, z) for this study was chosen as shown in Fig. 1. The bottom wall ($x = 0$) and the left ($y = 0$) and right ($y = 1$ m) vertical side walls ($0 < x < h$, ($h = 0.75$ m)) were maintained at a high temperature (T_H), which corresponds to the temperature of the furnace in a real crystal growth situation. The top wall was maintained at a lower temperature (T_C), which corresponds to the temperature at the solidification front, and the remaining vertical side walls ($h < x < 1$ m) were imposed with the zero heat flux boundary condition. The remaining lateral walls ($z = 0$, 1 m) of the cavity were also assumed to be thermally insulated (adiabatic). The thermal properties of this melt fluid were treated as constants. The above mentioned thermal boundary conditions can be used to model the synthetic production of single crystals, where the crystal grows slowly from a fluid nutrient contained in a crucible of variable geometry. The fluid under current investigation was incompressible and Newtonian along with the Boussinesq approximation made in the equations of motion along the gravity direction.

With the said assumptions, the governing equations to be solved are given below in the specified gravity field $g = (-g, 0, 0)$.

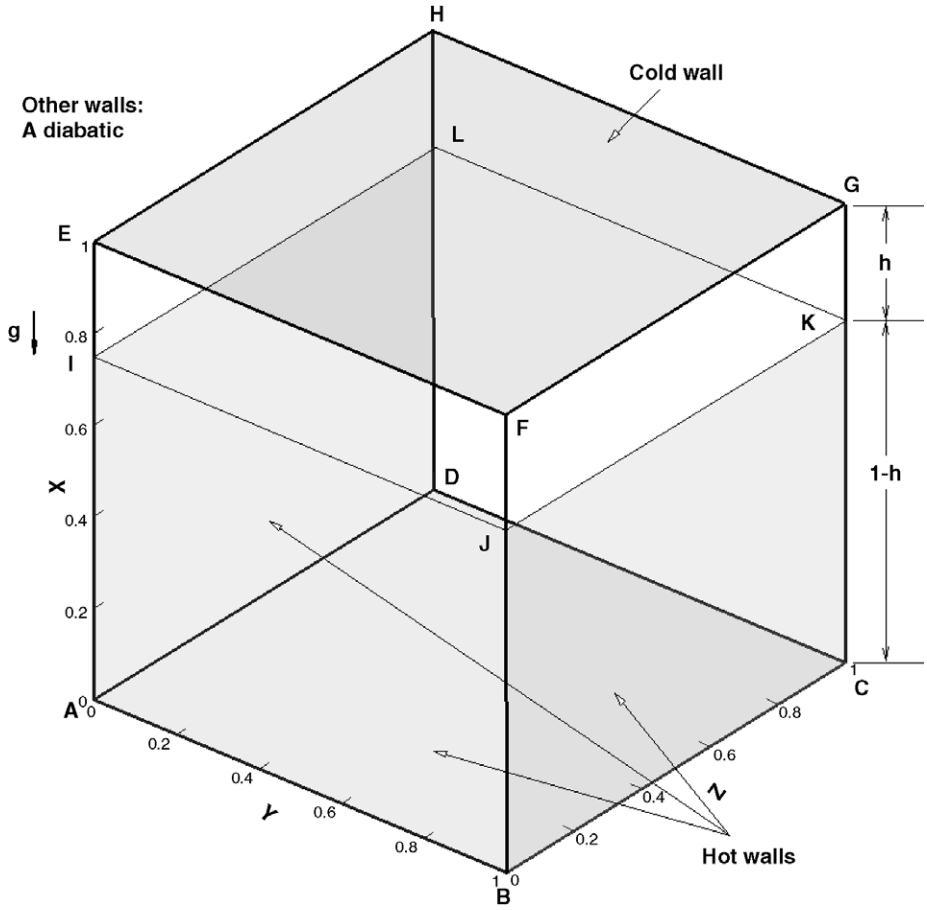

Fig. 1. Schematic of the investigated thermal driven cavity, where h (= 0.75 m) and g denote the height of the hot walls and gravity, respectively.

$$\nabla \cdot V = 0 \tag{1}$$

$$\frac{\partial V}{\partial t} + V \cdot \nabla V = -\nabla P + Pr\nabla^2 V + RaPrT \tag{2}$$

$$\frac{\partial T}{\partial t} + V \cdot \nabla T = \nabla^2 T. \tag{3}$$

In the above equations, $V = (U, V, W)$, t, P and T represent the dimensionless velocity vector along the (x, y, z) directions, time, pressure and temperature, respectively.

In the above Eqs. (1)–(3), the following non-dimensionalizations were employed $X = x/L$; $Y = y/L$; $Z = z/L$; $H = h/L$; $V = v\ L/\alpha$; $t = t'\alpha/L$; $p = p'L^2/\rho\alpha^2$; $T = (T' - T_C)/\Delta T$; $Pr = \nu/\alpha$ and $Ra = (g\beta_T \Delta T h^3)/(\nu\alpha)$, where t', p', T', ν, α and β_T denote the dimensional time, dimensional pressure, dimensional temperature, viscosity, thermal diffusivity and the coefficient of thermal expansion. Flow velocity was assumed to be of the no-slip type on the entire boundary of the domain. The temperature boundary conditions are given by

$$T(0, Y, Z) = 1$$

$$T(X, 0, Z) = T(X, 1, Z) = 1 \quad \text{for } 0 < X < H$$

$$\left(\frac{\partial T}{\partial X}\right)_{(X,0,Z)} = \left(\frac{\partial T}{\partial X}\right)_{(X,1,Z)} = 0 \quad \text{for } H < X < 1$$

$$T(1, Y, Z) = 0.$$

In the above nonlinear system, an attempt has been made to know the qualitative behavior of the fluid flow. In the mathematical terms, the number of non-wandering sets (including the fixed point, the limit cycle and the quasi-periodic or chaotic orbit) existing in the flow was determined. The appearance and the disappearance of such a non-wandering set is called bifurcation. Knowledge about the change of stability and the bifurcation, which always coincide in nonlinear dynamics, is thus a key to fully understand the currently investigated nonlinear differential system. One of our main objectives in conducting this study is to explore the flow and the thermal details using the flow topology, the stability analysis and the bifurcation analysis. Bifurcation is defined as a qualitative change in the nonlinear flow/thermal system. In the nonlinear flow topology, many bifurcation types can be discovered. In the present study attention was paid exclusively to the pitchfork bifurcations because of their existence in the currently investigated thermally driven cubical cavity.

3. Methodology and grid validation

Well established CFD package CFDRC [19], which provides a finite-volume flow solver, has been employed in the present study. The flow model geometry was constructed

using the grid generation software, namely, the CFD-GEOM. The flow volume, boundary and initial conditions for this model were set in the CFD-ACE solver. The third order upwind numerical method was used for the spatial derivatives. Conjugate Gradient Squared (CGS) method was employed as an effective acceleration means. In the final stage, the simulated results were viewed and analyzed by the 3D animated plotting tools like the CFD-VIEW and the TecPlot.

Grid independent tests were conducted based on the predicted L_2-error norms and the average errors for U and T to make sure that the computed solutions can represent the real flow physics. Fig. 2 shows the U and T solutions calculated at different meshes, namely, $21 \times 21 \times 21$, $41 \times 41 \times 41$ and $81 \times 81 \times 81$, for $Ra = 1 \times 10^5$. Figs. 2a and b show

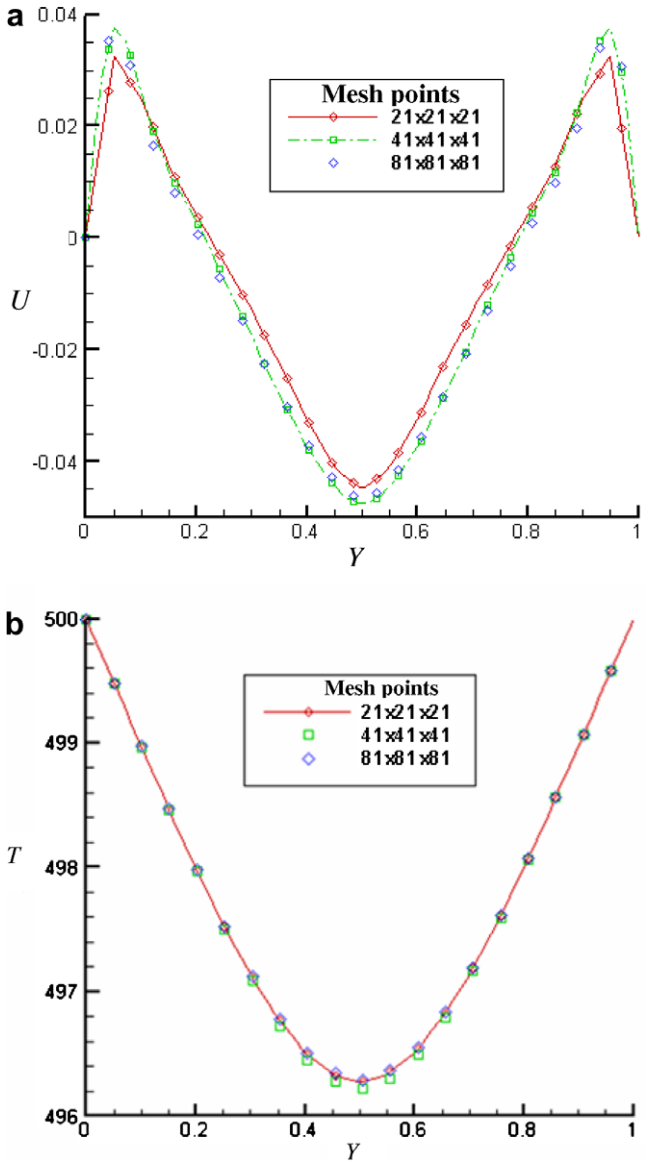

Fig. 2. Grid independent test at $Ra = 1 \times 10^4$. (a) Velocity u at the centre line (0.5, Y, 0.5) and (b) temperature T near the bottom surface (0.05, Y, 0.5).

Table 1
The computed L_2–error norms and average errors in a domain with $41 \times 41 \times 41$ and $81 \times 81 \times 81$ nodes at (0.5, Y, 0.5) and at (0.05, Y, 0.05) for U and T

		(0.5, Y, 0.5/0.05, Y, 0.5)
L_2-error norm	U	4.37734852E-04/2.19162510E-03
	T	3.87396403E − 02/1.17754256E − 02
Average error	U	4.77100462E − 02/9.19851574E − 02
	T	1.46493709E − 04/5.55973129E − 05

the u and T at the centre line (0.5, y, 0.5) and near the bottom surface (0.05, y, 0.5), respectively. From Fig. 2 it is observed that the currently employed $41 \times 41 \times 41$ uniform mesh results did not show much difference from those when the mesh resolution was increased or decreased by 50%. Table 1 shows the L_2-error norms and the average errors for U and T at $Ra = 1 \times 10^4$, with the reference mesh value of $41 \times 41 \times 41$. From Table 1 it is observed that the difference between the solutions obtained from $41 \times 41 \times 41$ and $81 \times 81 \times 81$ meshes is negligible. Hence the mesh with 41x41x41 resolution was used for simulations conducted in the investigated domain.

To initiate the non-symmetric steady-state mode (Mode 2) for the current Ra, the previous steady-state solution of Ra was considered as the initial solution (e.g., to compute the non-symmetric steady-state for $Ra = 2000$, the steady-state solution of $Ra = 1900$ was considered as the initial solution). To show that the simulated symmetry-breaking flows are indeed stable, the history of convergence behaviors for the velocity, pressure and temperature are provided in Fig. 3 at $Ra = 1.598 \times 10^4$. The iterative calculations of the primitive variables, such as velocity, temperature and pressure, were terminated when the residual norm criterion ($\leqslant 10^{-11}$) was reached for all the calculations.

4. Results and discussion

To begin with the flow topology is presented to give a global skeleton of the 3D flow development in the investigated cubical cavity. Then a symmetry-breaking or pitchfork bifurcation is asserted to take place in the range of $1 \leqslant Ra \leqslant 2.782 \times 10^5$. It was observed that this bifurcation occurred vertically (along the height of the cavity, h) and also diagonally. Hence the two sets of solutions, namely Modes I and II, were obtained. Extensive numerical verification was made to ascertain that the simulated pitchfork bifurcation was not of numerical origin. Having confirmed the existence of symmetry-breaking flow, the critical Ra range and the flow topology are presented in this paper.

4.1. Flow topology

In this section, the streamline portrait of the flow was constructed and subsequently the rigorous support was provided for the simulated streamline portrait by two ways.

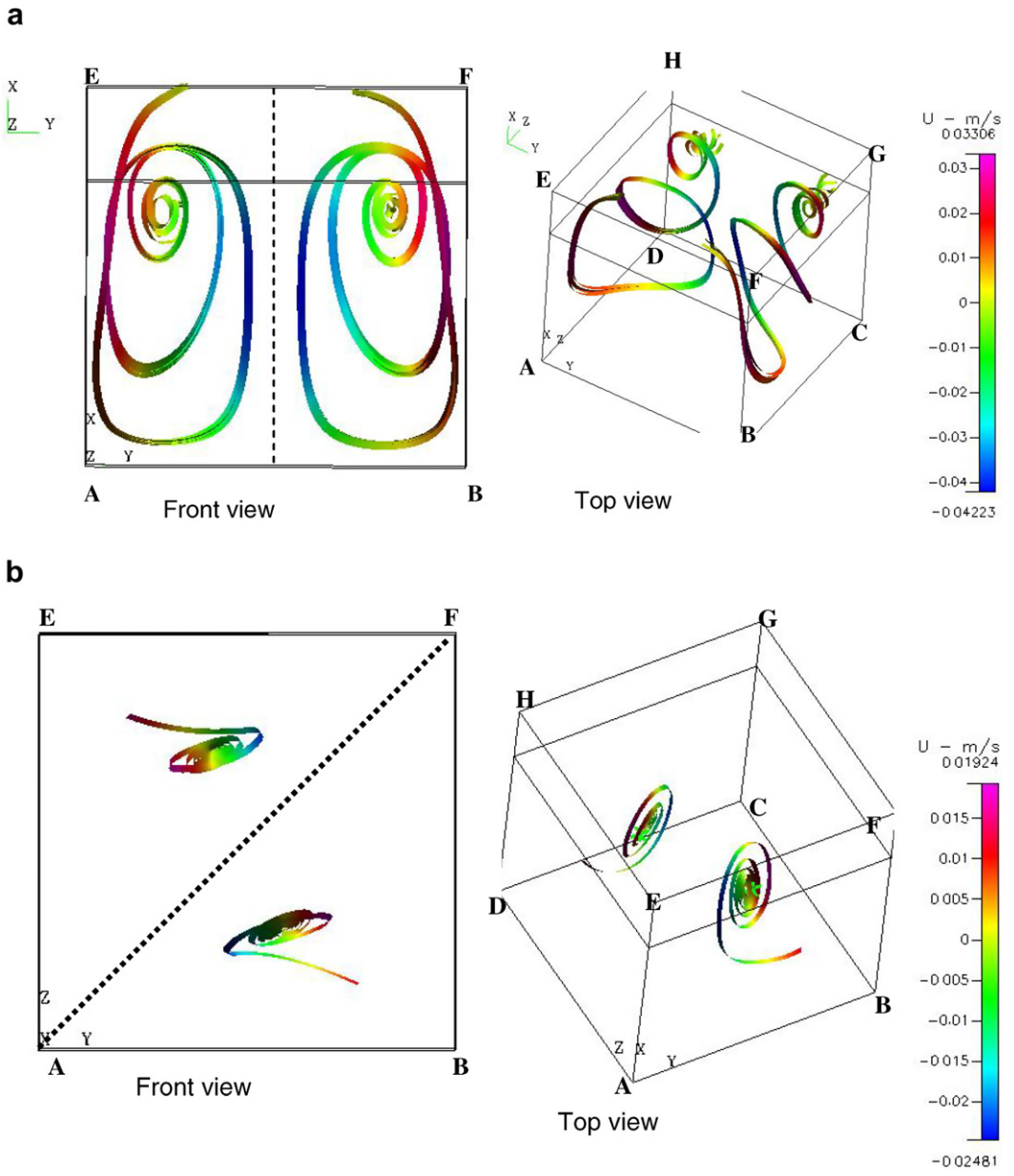

Fig. 3. A 3D illustration of two modes of the simulated streamtraces at $Ra = 1 \times 10^4$. (a) Mode I and (b) Mode II.

One was by invoking the topological constraints and the structural stability criteria and the other by listing the corroborative numerical evidence.

4.1.1. Corroborative evidence for the proposed streamline portrait

Determination of the stream-function is one way to construct a streamline portrait of the flow (flow skeleton) [20]. This map contains the critical points and the limiting fluid particle trajectories that can well characterize the flow. The flow skeleton was presented in the transverse sections. These 3D stream-function sections correspond to the 3D stream-tubes in the transverse cuts and are equivalent to the 3D trajectories of the fluid particles into the reduced coordinate system. Mathematically speaking, these fluid trajectories are the flow domain fibers and constitute a local vector bundle [21].

The topology constraint is based on the Euler number ξ of the flow. As explained by Jana et al. [22] the Euler number of a surface is defined as the sum of the Poincare indices of the critical points on the surface. A Poincare index of the hyperbolic point is -1, a parabolic point is $-1/2$, and an elliptic point is 1. The topological invariance relation is given by the following rule of Hunt

$$E - \left(H + \frac{1}{2}P\right) = \xi = 0 \tag{4}$$

where E, H, P represent the number of elliptic points, hyperbolic points and parabolic points, respectively. The topological rule given by Eq. (4) does not guarantee the

existence of a physically relevant flow. Rather, it is merely a way to check for the topological consistency [23]. One can also validate the approximated velocity field by pursuing the fact that the kinematics of a physically realizable flow is related to its stability. Instead of referring to the stability of the ideal flow, in the current study attention was focused on the structural stability of the multiple solutions, namely Modes I and II, with the infinitesimal changes to the geometry and the boundary conditions in the currently investigated cubical cavity. Drazin and Reid [24] defined a structurally stable system as the one that does not change its qualitative solution character subjected to the infinitesimal changes in the geometrical setting of a system and the physical parameters of the working fluid and the specified boundary conditions.

The 3D flow paths of Mode I and Mode II orientations can be best illustrated by virtue of the simulated stream-traces. In Fig. 3 it is observed that the stream-traces in both Modes exhibit the symmetric nature. The Mode I and Mode II show the symmetric nature with respect to the transverse and diagonal planes, respectively. Mode I results illustrate that at one rear end of the adiabatic wall ($Z = 1$), the apparent spiraled stream-traces are present and they lead to the formation of eddies near that adiabatic wall. This is due to the fact that the heat flux was convected towards the adiabatic wall, $Z = 1$. From Mode II results it is observed that an increasingly apparent spiraling nature of the stream-traces at the centre of the cavity is present. The formation of such eddies at the centre of cubical cavity is due to the heat transfer convected in the centre of cavity. The heat transfer results for the Mode I and Mode II have been discussed in detail in the later part.

The 2D flow skeleton in Fig. 3 represents the (X, Y)-plane (or transverse section) of the Mode I and Mode II orientations. Figs. 3a and b are the two projections of the vector bundle. Two recirculating cells, namely CI and CII, were observed in the Mode I and Mode II solutions. These cells correspond to the two counter-rotating helical vortices in the double helix topology. In the following discussion and in the rest of the article, the following terminology is used to distinguish these two vortices. By considering the transverse section of the stream-function presented in Fig. 3, the rotation of the fluid in the clockwise-direction is referred as CI, while the rotation of the fluid in the anti-clockwise direction is referred as CII. CI encloses the elliptic point (E_1) for the Mode I and (E_1, E_2) for the Mode II. CII encloses the elliptic point (E_2) for the Mode I and (E_3, E_4) for the Mode II. Both CI and CII regions are of the same size.

In Fig. 3a CI and CII cells form a closed pattern with the parabolic points denoted as P_1 and P_2. Also CI and CII cells are delineated from each other by the parabolic points, namely, P_3 and P_4. The Mode II streamline portrait in Fig. 3b shows that the cells CI and CII are bounded by a set of parabolic points (P_1, P_6) and (P_4, P_5), respectively. There exists a hyperbolic point (H) between the repeating cells. In the remaining flow region there exist two more parabolic points (P_2, P_3). The representation of geometric objects in the reduced coordinates is further clarified in the next paragraph by relating the 3D structure to the 2D cuts.

It is useful to describe the streamline portrait in terms of the dynamical system nomenclatures. By comparing the 3D plot in Fig. 3 with the projections depicted in Fig. 4, it becomes clear that the boundary of CI cell is a 2D manifold heteroclinic to the two invariant one-dimensional manifolds passing through the point P_1 for Mode I (Fig. 4a) and points (P_1, P_6) for Mode II (Fig. 4b). The two one-dimensional manifolds form the two helices on the outer surface. Similar topology characterizes the boundary of cell CII which passes through the point P_2 for Mode I (Fig. 4a) and the points (P_4, P_5) for Mode II (Fig. 4b).

Based on the global geometrical constraints, the streamline portrait obtained from the analytical approximation, in Figs. 4a and b, is 'realistic'. Quite obviously, the critical points in the streamline portrait presented in Fig. 4a satisfy equation (6) with the two elliptic points ($E = 2$) and four parabolic points ($P = 4$). Similarly, the critical points in Fig. 4b satisfy the topological rule given in equation (6) with the four elliptic points ($E = 4$), one hyperbolic point ($H = 1$) and six parabolic points ($P = 6$).

The flows depicted in Figs. 3a and b are structurally stable according to the theorem given in the work of Ma and Wang [25]. Indeed, the conditions for the structural stability criteria of the divergence-free vector fields that satisfy the Dirichlet boundary conditions (no-slip at the walls) are met with. The velocity field is found to be sufficiently regular for the Mode I and Mode II orientations. Both parabolic points, P_1 and P_2 shown in Fig. 4a, are connected with the stable manifolds. Similarly for Mode II, the parabolic points P_2 and P_6 shown in Fig. 4b are connected with the stable manifolds. Such manifolds correspond to the flow regions which separate the counter-rotating cells and become visible as lines. These lines act as barriers for the two vortices when the flow is observed from the transverse and diagonal planes for the Mode I and Mode II, respectively (Fig. 3). By verifying that the simulated flow structure is structurally stable, the fidelity of the simulated thermal and velocity fields was further corroborated from the available results in the literature.

4.1.2. Corroborative numerical evidence

The 2D square cavity benchmark solutions of de Vahl Davis [26] and Le Quéré [27] were compared with the present calculations, which were carried out in a 41×41 non-uniform mesh with more grid points near the bounding walls. The agreement was found to be satisfactory as shown in the following Table 2. To present more validation, the solutions obtained at $Ra = 10^6$ and some reference values are compared and are tabulated in Table 3. The locations for the maximum velocities are calculated and compared. The present results shown in Table 4 for U_{max} and W_{max} are in good agreement with the results by Wakashima and Saitoh [28] and others.

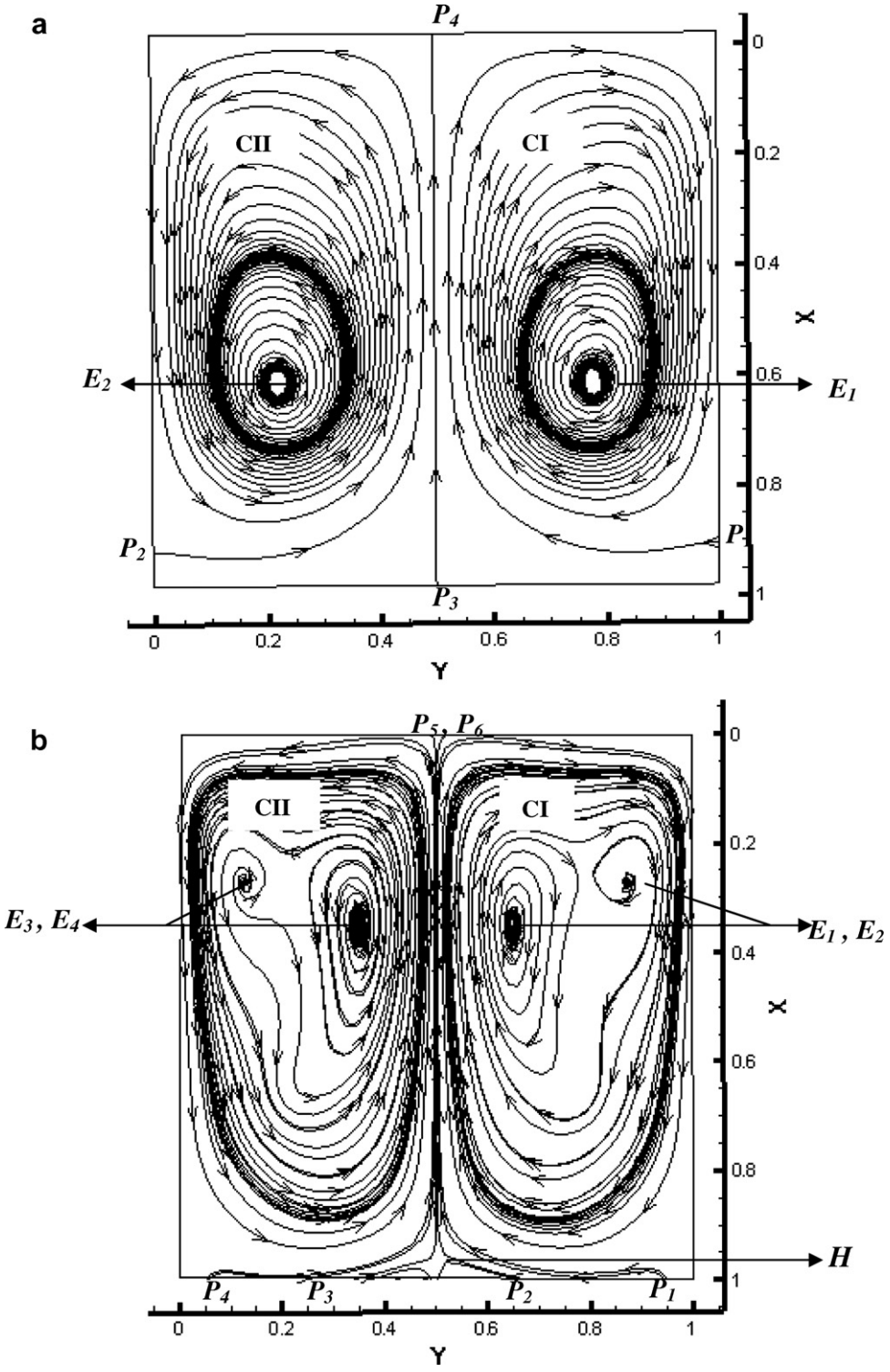

Fig. 4. The simulated streamlines and critical points at the cross-flow plane $z = 0.5$ for $Ra = 1 \times 10^5$. CI, CII represent the clockwise-rotating cells and anti-clockwise-rotating cells. E, H and P denote the elliptic, hyperbolic and parabolic points, respectively. (a) Mode I and (b) Mode II.

The 3D cavity considered by Wakashima and Saitoh [28] had an aspect ratio of unity and was filled with the working fluid of air. The Prandtl number was fixed at 0.71. The vertical walls located at $X = 0$ and $X = 1$ were retained to be isothermal but at hot and cold temperatures, respectively. The remaining four sidewalls are taken as adiabatic. The agreement of the present results with Wakashima and Saitoh [28] is shown in the following Table 4 for the U_{max} and W_{max} and is found to be satisfactory.

The 2D and 3D numerical results of Wan et al. [31] and Bennacer et al. [11] were compared with the presently predicted results. Wan et al. [31] have considered a differentially

Table 2
Comparison of the 2D results of de Vahl Davis [26] and Le Quéré [27]

		Ra			
		10^3	10^4	10^5	10^6
Present	$U_{max}(1/2,z)$	3.649	16.178	34.7295	64.629
		0.813	0.823	0.855	0.850
	$W_{max}(x,1/2)$	3.697	19.617	68.59	219.36
		0.178	0.119	0.066	0.0379
de Vahl Davis [26]	$U_{max}(1/2,z)$	3.649	16.178	34.73	64.63
		0.813	0.823	0.855	0.850
	$W_{max}(x,1/2)$	3.697	19.617	68.59	219.36
		0.178	0.119	0.066	0.0379
Le Quéré [27]	$U_{max}(1/2,z)$	–	–	–	64.83
					0.850
	$W_{max}(x,1/2)$	–	–	–	220.6
					0.038

Table 3
Comparison of the present solutions with the reference solutions computed at $Ra = 10^6$

$Ra = 10^6$	$U_{max}(z)$	$W_{max}(x)$
Present	0.08128 (0.8500)	0.2379 (0.0500)
Fusegi et al. [29]	0.08416 (0.8557)	0.2588 (0.0331)
Janssen et al. [30]	0.08099	0.2585
Wakashima and Saitoh [28]	0.08129 (0.8500)	0.2382 (0.0500)

heated, closed square cavity whose left and right vertical walls are maintained to be hot and cold, respectively, and the horizontal walls are adiabatic. In Table 5 the predicted results were compared with the predictions of Bennacer et al. [11], whose investigated geometry is similar to the present study. Table 5 tabulates the Nusselt number (Nu) values against Ra at the bottom, left and top surfaces. Comparison results are found to be satisfactory. From Table 5 it is observed that increasing Ra modifies the flow intensity without significantly affecting the overall heat transfer but it does modify the ratio between the lateral and lower surface contributions.

For a 3D heat transfer flow in the rectangular enclosure with $Pr = 1$ and aspect ratios $A = A_X = A_Y = 2$ and 6, the present results show the critical Rayleigh numbers as 2085 and 1755, respectively, which coincide with the results of Gelfgat [32]. For the convective flow in an air cubical enclosure heated from below, the first and second primary bifurcations occur at $Ra \cong 3389$ and 5900, respectively. These critical Ra values coincide with the results of Puigjaner et al. [33], who have considered the calculation domain, which is scaled by the length of the side of the cubical cavity and the temperatures at the top and the bottom horizontal walls are constant and equal to cold and hot temperatures, respectively.

The local heat transfer iso-contours at the bottom horizontal surface ($X = 0$) for $Ra = 10$ and 3000 were compared with the results of Bennacer et al. [11] and are shown in Figs. 5a and b, respectively. It is observed that the predicted heat transfer results agree well with the results of Bennacer et al. [11]. The symmetric regions in Figs. 5a and b exhibit the increasing flow intensity with the Rayleigh number. Also Fig. 5 represents the four different situations: The maximum temperature gradient is in the middle due to the imposed thermal boundary conditions. For the lower Ra(= 10), a distributed temperature field was exhibited. For the intermediate Ra(= 3000), the increase in the flow induces a higher local heat transfer rate

Table 4
Comparison of the present solutions with those of Wakashima and Saitoh [28]

	Ra and Grid size	$U_{max}(z)$	$W_{max}(x)$
Present	$Ra = 10^6$ 0.025	0.08128 (0.8500)	0.2379 (0.0500)
Wakashima and Saitoh [28]		0.08129 (0.8500)	0.2382 (0.0500)
Present	$Ra = 10^5$ 0.025	0.1423 (0.8500)	0.2406 (0.0751)
Wakashima and Saitoh [28]		0.1423 (0.8500)	0.2407 (0.0751)
Present	$Ra = 10^4$ 0.025	0.1989 (0.8250)	0.2211 (0.1253)
Wakashima and Saitoh [28]		0.1989 (0.8250)	0.2211 (0.1253)

Table 5
Comparison of the Nu values obtained at the bottom, left and top surfaces against Ra

Nusselt number (Nu)					
Ra		10^2	1×10^3	2×10^3	3×10^3
Bottom surface (ABCD)	Bennacer et al. [11]	0.260	0.279	0.304	0.310
	Present	0.26018	0.28061	0.30438	0.31148
Left surface (ADIL)	Bennacer et al. [11]	0.69	0.69	0.686	0.684
	Present	0.6918	0.6951	0.6783	0.6721
Top surface (EFGH)	Bennacer et al. [11]	−2.10	−2.12	−2.13	−2.14
	Present	−2.1052	−2.1077	−2.1134	−2.1308

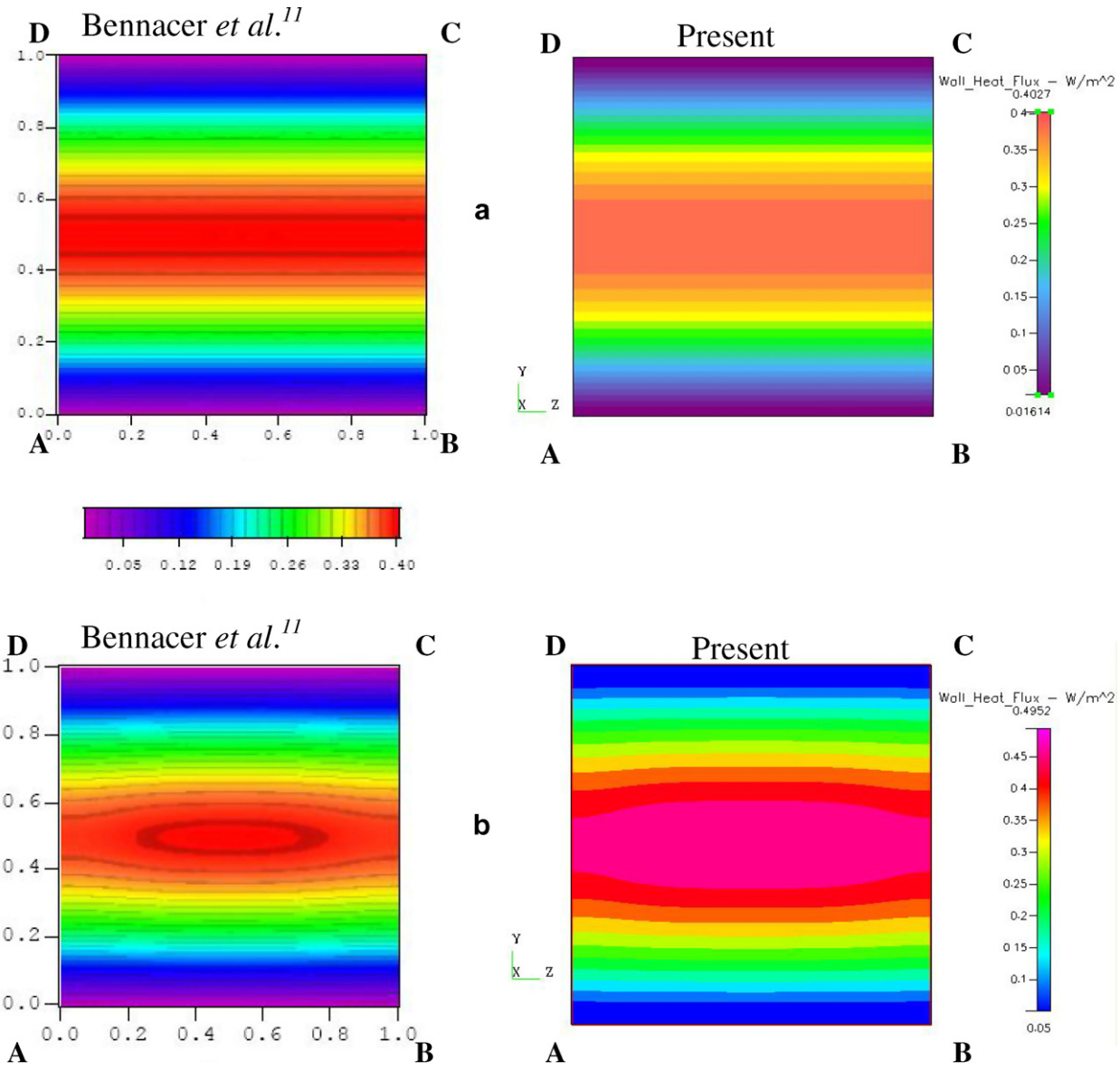

Fig. 5. Comparison of the simulated local contours of Nusselt number (*Nu*) on the hot plane (ABCD) with those of Bennacer et al. [11]. (a) $Ra = 10$ and (b) $Ra = 3000$.

(*Nu*) along the centreline due to the arrival of the cold fluid. Close to the hot walls ($Y = 0$ and 1) the local heat transfer rate was observed to be small due to the flow damping.

4.2. Flow field description

Having corroborated the present numerical results, the local behavior of the pitchfork bifurcation is analyzed based on the heat flux and *U*-velocity iso-contours. To effectively obtain a profound understanding of the buoyancy driven convective flow features, the wall heat flux on various planes were calculated at $Ra = 1 \times 10^4$. Fig. 6 shows the wall heat flux distribution for the two sets of solutions, the Mode I and Mode II. From Fig. 6, it is observed that the simulated heat flux has its peak value near the bottom surface and minimum at the top. It is natural to observe the asymmetric local heat flux distribution between the hot and cold walls as there exists a steady-state asymmetric distribution in the flow and thermal fields. There was a large amount of heat, transferred from the lower bottom of the hot wall, to the fluid. This rate of heat transfer from the wall to the fluid, and vice versa, is increased with *Ra*. Also, the Mode I heat flux elucidates that the heat is convected asymmetrically towards one partially heated vertical wall (ABEF). Mode I has symmetric nature about $Y = 0.5$ plane but not with respect to the $Z = 0.5$ and the diagonal planes. Mode II heat flux shows that the heat is distributed symmetrically about the diagonal plane but is asymmetric with respect to *Y*, $Z = 0.5$ planes. The contours in the adiabatic walls indicate that there is no movement of heat flow through this boundary. In the immediate neighborhood of the hot and cold walls,

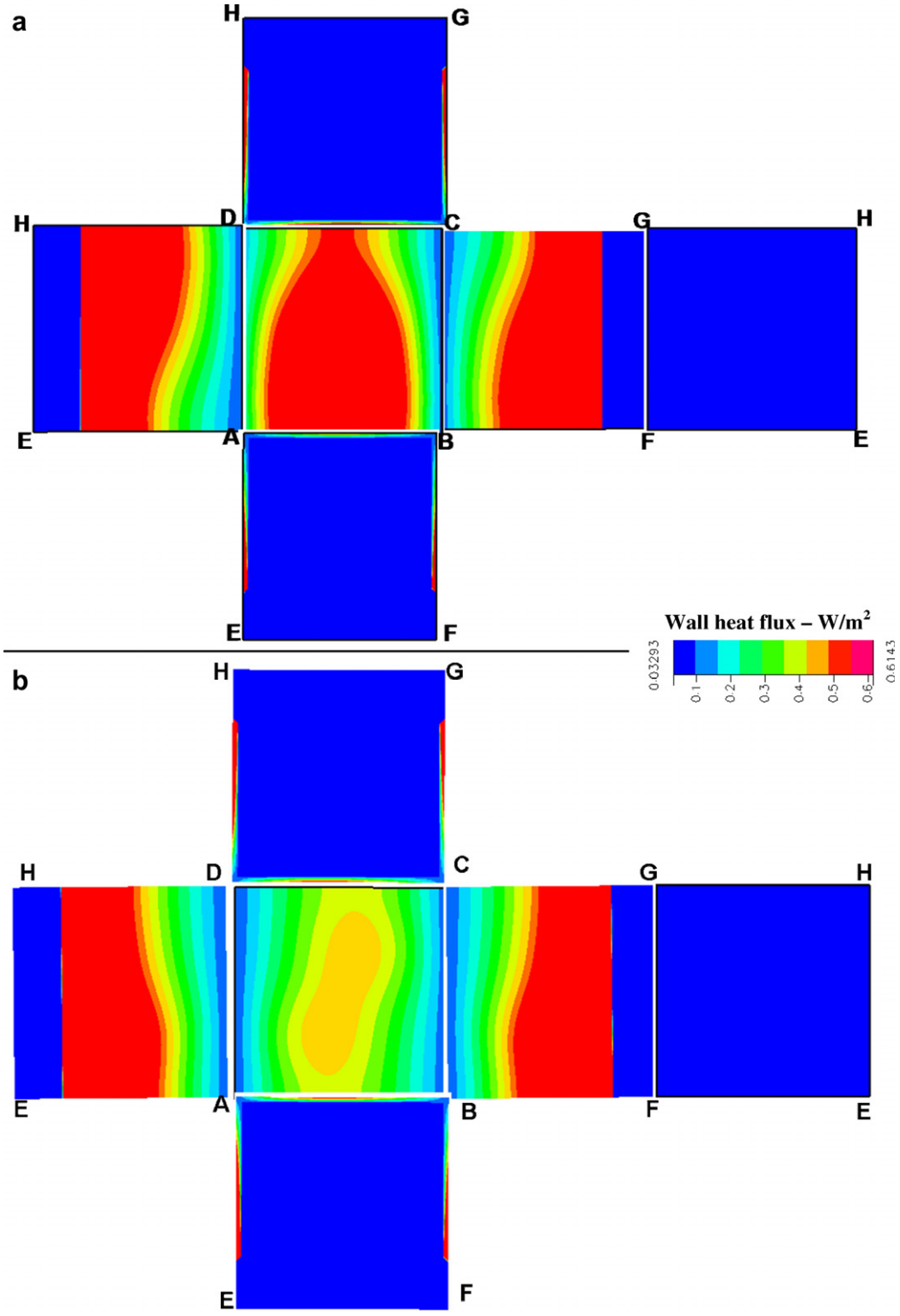

Fig. 6. A 3D illustration of two possible surface flow topologies based on the simulated iso-contours of the wall heat flux obtained at $Ra = 1 \times 10^4$. (a) Mode I and (b) Mode II.

the contours remain parallel to the isothermal vertical walls.

Fig. 7 plots the U-velocity iso-contours on different cutting planes at $Ra = 1 \times 10^4$. Both the Mode I and Mode II flows exhibited an asymmetric behavior. For the Mode I solution, the existence of two eddies at the transverse plane and three eddies at the Z and diagonal planes were observed. In the Mode II solution three eddies were, however, noticed at all the planes. The Mode I solution pattern exhibits the asymmetric behavior with respect to the Y,

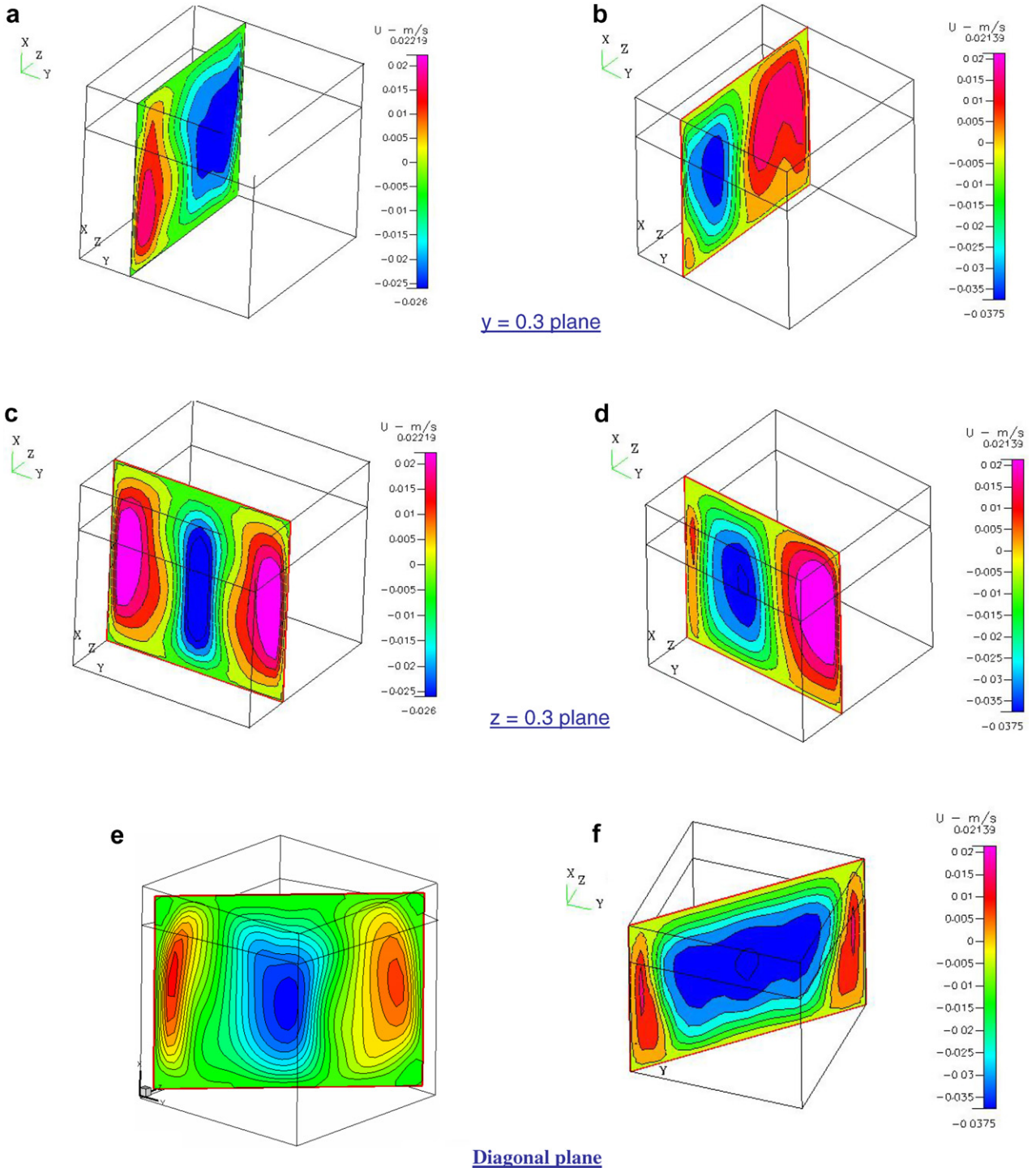

Fig. 7. The simulated U-velocity iso-contours on $Y = 0.3$, $Z = 0.3$ and the diagonal planes at $Ra = 1 \times 10^4$. (a, c and e) Mode I and (b, d and f) Mode II.

$Z = 0.3$ and the diagonal planes. As the flow was gradually evolved to exhibit the Mode II bifurcation feature, the velocity on the diagonal plane remained relatively invariant with the exception at the $Y = 0.5$ and $Z = 0.5$ planes. Unlike the Mode II bifurcated flow, the discrepancy in the flow nature between the two halves of the channel (*i.e.*, $Y,\ Z < 0.5$; $Y,\ Z > 0.5$ and diagonal plane) in the Mode I flow is clearly observed. The Mode II solution showed, however, the asymmetric behavior with respect to the $Y,\ Z = 0.3$ planes and symmetric behavior along the diagonal plane. The local heat transfer and the velocity iso-contours (Figs. 6 and 7) on the bottom wall correspond to the rotation of the main cells inside the cavity about the three planes, namely, the diagonal, Z and Y planes. The existence of a wide range of fluid flow and heat transfer characteristics in such a simple geometry, where the

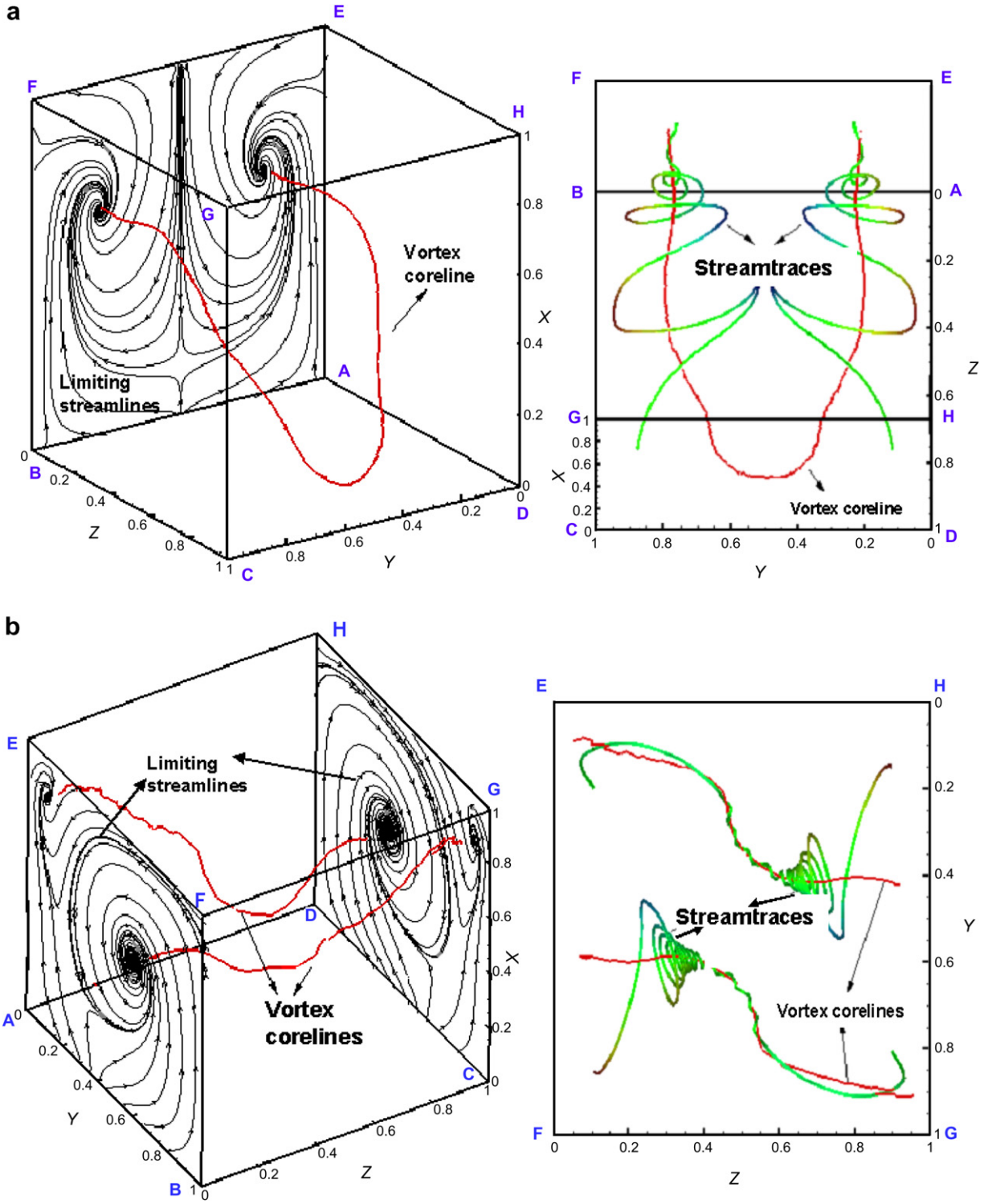

Fig. 8. The simulated vortex corelines, limiting streamlines and streamtraces for the case considered at $Ra = 1 \times 10^5$. (a) Mode I and (b) Mode II. The color contours of velocity streamtraces are shown in Fig. 8.

patterns are dictated purely by the buoyancy force, is particularly absorbing.

The vortex corelines are regarded as the main signature of the vortical flow. Generally, a swirling motion in the fluid is regarded as the vortex. Robinson [34] provided the definition for vortex as "A vortex exists when instantaneous streamlines mapped onto a plane normal to the vortex core exhibit a roughly circular or spiral pattern, when viewed from a reference frame moving with the center of the vortex core." An attempt was made to obtain the

profound vortex flow nature in the present cubical cavity flow for the Mode I and Mode II orientations.

Figs. 8a and b show the symmetrical vortex corelines in the Mode I and Mode II orientations along with the limiting streamlines (Chiang et al. [35]) and streamtraces. The vortex corelines are drawn according to the velocity gradient eigenMode method [36]. An important feature of the vortex coreline is the complex surface streaking pattern. By definition, the spiraling vortex motion has its origin/end from the bounding end walls. Hence in Fig. 8 the limiting streamlines are drawn to observe the evolution of these corelines in the vicinity of the end walls. Fluid particles near the end walls could have caused the vortical flow to develop in the third dimension. In the Mode I flow, there exists only one vortex coreline which is symmetric about the $Y = 0.5$ plane. The Mode II flow consists of two vortex corelines which are anti-symmetric to each other. The vortical corelines of Mode I and Mode II orientations have their origin/end points on the adiabatic walls. A very strong predominant vorticity nature was found to occur in the regions very close to the flanks of the two adiabatic end walls. It is observed from Fig. 8b that the limiting streamlines exhibited the anti-symmetric nature on the flanks of the adiabatic end walls. Also it is observed from Fig. 8a that a more apparent spiraling nature of the streamlines existed near the end wall than that in the centre of the cavity. This implies that the vorticity is sturdy near the end walls. In Fig. 8b the Mode II orientation shows that the vorticity is sturdy in the centre of the cavity due to the more apparent spiraling nature of the streamlines existing in the centre of the cavity.

4.3. The route of developing pitchfork bifurcation

As mentioned earlier, the pitchfork bifurcation is of the static and local type and involves one or more equilibrium solutions. Usually the nonlinear systems with the geometry and the flow symmetry perturbations of different sorts may initiate pitchfork bifurcation. The currently investigated 3D natural convection problem is featured with two possible symmetric conditions in the geometry as well as the boundary conditions. Symmetry was seen with respect to the transverse and diagonal planes. As a result, it was expected to observe two modes (Modes I and II) of pitchfork bifurcation in the current nonlinear partial differential system governed by Eqs. (1)–(3) as the system control parameter Ra was increased beyond its critical value. As the solution is started to bifurcate, the geometrically symmetric cavity fluid flow lost its symmetry and the stable branch became unstable. This led to the formation of two new stable branches. Hence this pitchfork bifurcation solution is called as the symmetry-breaking solution.

The critical nature of the Mode I and Mode II solutions that vary with respect to Ra was studied based on the predicted L_2-error norms. The entire Mode I solutions were found to be asymmetric with respect to $Z = 0.5$ and the diagonal planes. The solution was switched, however, from the symmetric to asymmetric patterns for the various critical Ra values at the $y = 0.5$ plane. Hence the L_2-error norms for the U, V, W, P and heat flux were calculated for the Mode I solution at the $Y = 0.5$ plane and are plotted in Fig. 9 against Ra. This figure clearly illustrates the evolution of the pitchfork bifurcation along the Y (= 0.5) plane in the range of $10^3 \leqslant Ra \leqslant 10^5$. Initially, for $Ra \leqslant 10^3$ the L_2-error norm was very close to zero. This implies that the flow was symmetric for $Ra \leqslant 10^3$(steady I). As Ra was increased further ($\geqslant 10^3$), the increasing L_2-error norm values were seen. Under these circumstances the solution was denoted as steady III. (The Mode II steady-state solution was denoted as steady II). These results imply that the pitchfork bifurcation started to evolve around $Ra = 6740$ and was retained until $Ra = 8970$ (steady IV). When the value of Ra was increased further, the L_2-error norms were found to be very close to

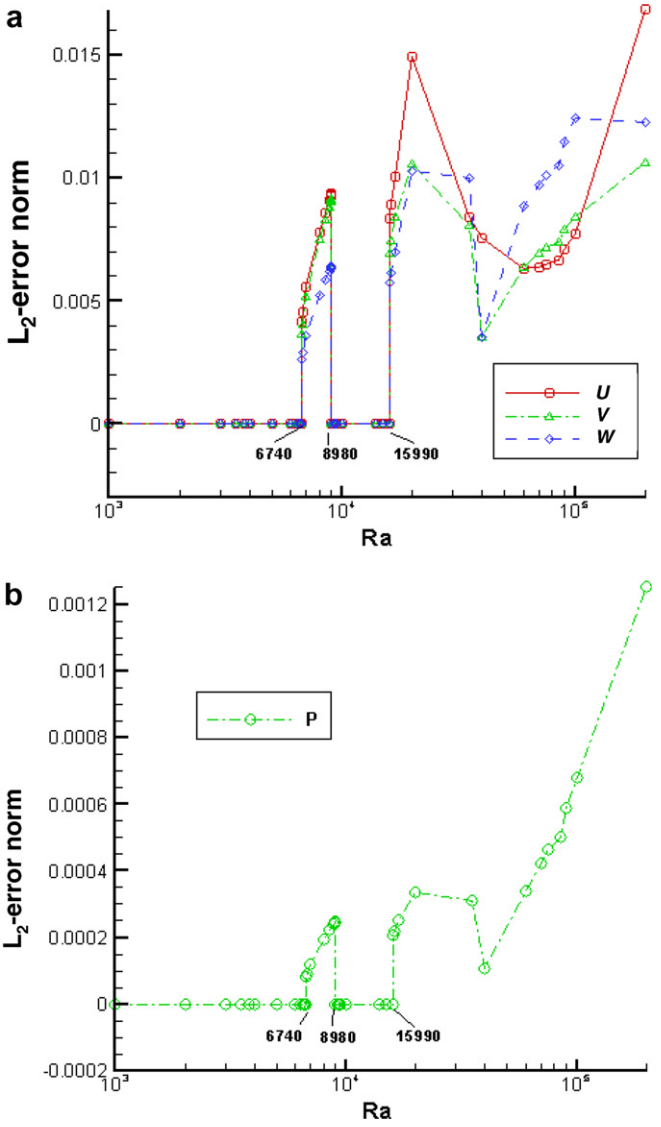

Fig. 9. The plots of the simulated difference, cast in L_2-error norms with respect to the $Y = 0.5$ plane, for the flow variables (a) U, V, W and (b) P for illustrating the presence of pitchfork bifurcation in the Mode I flow.

zero. This indicates that the flow becomes symmetric again. For $Ra \geqslant 10^4$, larger error was found in comparison with the previous one. Hence the pitchfork bifurcation (steady V) started to evolve again when the value of Ra was increased above 15990. All the Mode II solutions exhibited symmetric nature along the diagonal plane and asymmetric nature along the Y, $Z = 0.5$ planes. The L_2-error norm values of the U, V and W were not changed until the steady-state IV was reached. Beyond $Ra = 15{,}990$, the L_2-error norms of these velocities were found to deviate from each other. TheL_2-error norm of the pressure (P) was found to be small in comparison with the velocity values shown in Fig. 9b. It is also observed that the alternate symmetric and asymmetric nature of the pressure field is the same as the velocity.

Figs. 10a, b and c illustrate the oscillatory nature of the flow from the symmetric to asymmetric nature. By adding a small perturbation by an amount of $\Delta Ra = 10$ on the unperturbed cell predicted at $Ra = 6730$, the flow started to show the asymmetric nature (Fig. 10a) and was switched from the steady-state I to the steady-state III. Hence the first critical pitchfork bifurcation Ra (Ra_{CP1}) value was observed at 6740. Also, the break of symmetry leads to a slight growth of one of the vortices and a slight decay of the other. This secondary steady-state branch consisted of symmetric vortices, which were separated by the heteroclinic lines connecting the hyperbolic fixed points of the flow. This branch had created tertiary steady-states for which the contours of the flow were changed such that the middle points of the neighboring co-rotating vortices were shifted up and down. With further increase of the Rayleigh number, the non-symmetric flow pattern continuously transforms, thereby tilting the vortices up and down.

The flow pattern starts to show the symmetric nature again as shown in Fig. 10b. Hence, another pitchfork bifurcation occurred (steady IV) at $Ra_{CP2} = 8970$ (Fig. 10b) and it was stable within an interval $8970 \leqslant Ra \leqslant 15990$. By adding a small perturbation by an amount of $\Delta Ra = 10$ on the perturbed cell predicted at $Ra_{CP2} = 8970$, the flow is switched from the asymmetric steady-state III to the symmetric steady-state IV as shown in Fig. 10b. The solutions were returned to exhibit the symmetric vortices and the solutions were stable until the third critical pitchfork bifurcation was found at $Ra_{CP3} = 15990$. The third pitchfork bifurcation (steady V) is illustrated in Fig. 10c. For the value of Ra beyond Ra_{CP3}, the symmetric nature was lost and both solution modes (Modes I and II) exhibited the same set of results *i.e.,* the disappearance of the multiple solutions at $Ra = 45000$. The present predicted critical Ra values are found to be closer to the 2D results predicted by Ganaoui and Bontoux [37] and Bennacer et al. [11].

Fig. 11 illustrates the topology of pitchfork bifurcation with the increasing Rayleigh numbers. In Fig. 11 the contours of the U-velocity are plotted for various Rayleigh numbers. Initially for $Ra \leqslant 6730$ the flow exhibited a symmetric nature, as shown in Fig. 11i, and is denoted as steady II. There exist two corner vortices and one centre vortices, which are symmetric with respect to the $Y = 0.5$ plane. When Ra was increased above 6730, the symmetry was lost and the break of symmetry leads to a slight growth of the centre vortex and a slight decay of the others. The two corner vortices become closer to the edges near the mid-plane $Y = 0.5$ compared to those for $Ra \leqslant 6730$. With further increase of the Rayleigh number, the non -symmetric flow pattern continuously transforms. The totally deformed nature of the vortices is observed until $Ra = 8990$ and this range is denoted as the steady III (Fig. 11ii). The existence of the steady symmetry-breaking pitchfork bifurcation shows multiple symmetry and asymmetry steady-states. Thus, there exists at least one symmetric and non-symmetric steady-state. When Ra was amplified further, then the flow retains its symmetric nature at 15980. Fig. 11iii shows the symmetric flow with respect to the $Y = 0.5$ plane. The two corner vortices become closer to the edges of y plane and retain their respective symmetry with respect to the mid-plane of $Y = 0.5$ compared to the previous steady III. This symmetric steady nature of the flow remained until $Ra < 15{,}990$ and this range is denoted as the steady IV. The final pitchfork bifurcation showed its presence when Ra was augmented to 15990. Once again the flow symmetry was lost as shown in Fig. 11iv and this steady-state is denoted as the steady V. Also the multiple steady-state disappears at $Ra = 45{,}000$, but the non-symmetric flow is retained.

A complete overview of all the solution branches is presented schematically in the global pitchfork bifurcation diagram (Fig. 12) at the $Y = 0.5$ plane against the Rayleigh number. In Fig. 11 the present simulations of the five symmetric/asymmetric steady-states, multiple solutions for the critical Ra values are shown. Fig. 12 has a close similarity to the Feigenbaum sequence [38] that is normally employed to describe the route to chaos. In the terminology of Mitchell Feigenbaum, there exist some critical Rayleigh numbers at which the characters of Feigenbaum sequences change sharply. The first bifurcation ($Ra < 3040$) is the transition of the system behavior from the basic symmetric steady-state solutions. For $Ra = 3040$, the sequence asymptotes to a stable fixed point. The value of $Ra = 3040$ is critical for the onset of convection, at which the system bifurcates from one fixed point to two stationary solutions, namely, the Mode I and Mode II. Both of the solutions are predicted to be physically possible in the cavity in the sense that they satisfy Eqs. (1)–(3). For the value of Ra beyond 3040, the primary steady-state lost its stability and produced two steady-state orientations, namely steady I and steady II for Modes I and II, respectively. Further, there are three critical values of Ra, namely $Ra_{CP1} = 6740$, $Ra_{CP2} = 8970$ and $Ra_{CP3} = 15{,}990$, which lead to the first, second and third pitchfork bifurcations, respectively. These bifurcations are explained in detail in Figs. 10 and 11. The multiple solutions disappeared at a value around $Ra = 45000$.

These results indicated that, over a range of Ra, at least two stable steady-states existed. From an experimental

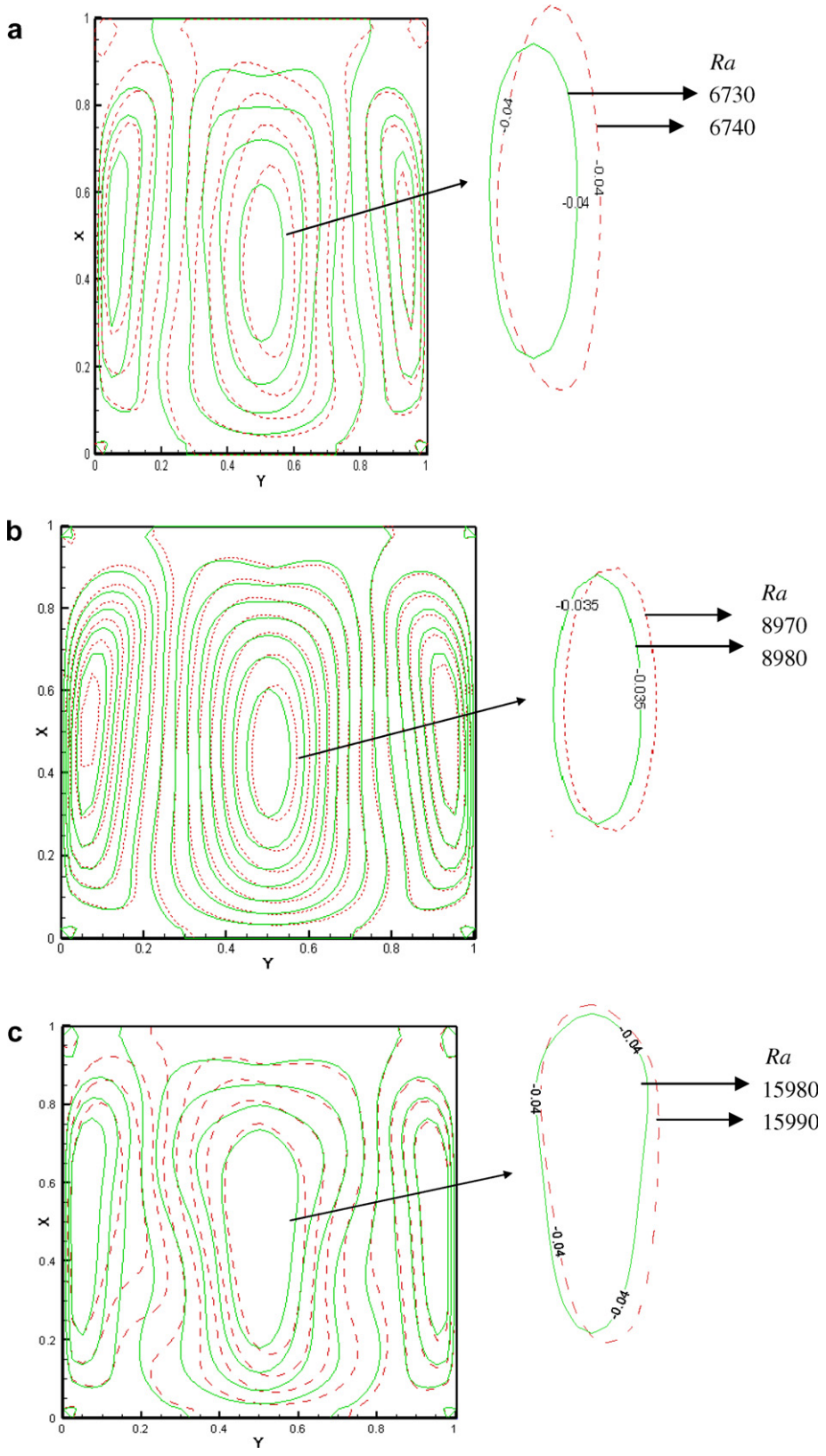

Fig. 10. Illustration of the pitchfork bifurcation. The numbers denote the contour levels. Solid and dotted lines denote the symmetric and asymmetric contours, respectively.

point of view, the existence of multiple steady-states implies that the markedly different behaviors may be obtained under the same condition, depending on which solution branch is accessed (Sonda et al. [39,40]). Then at

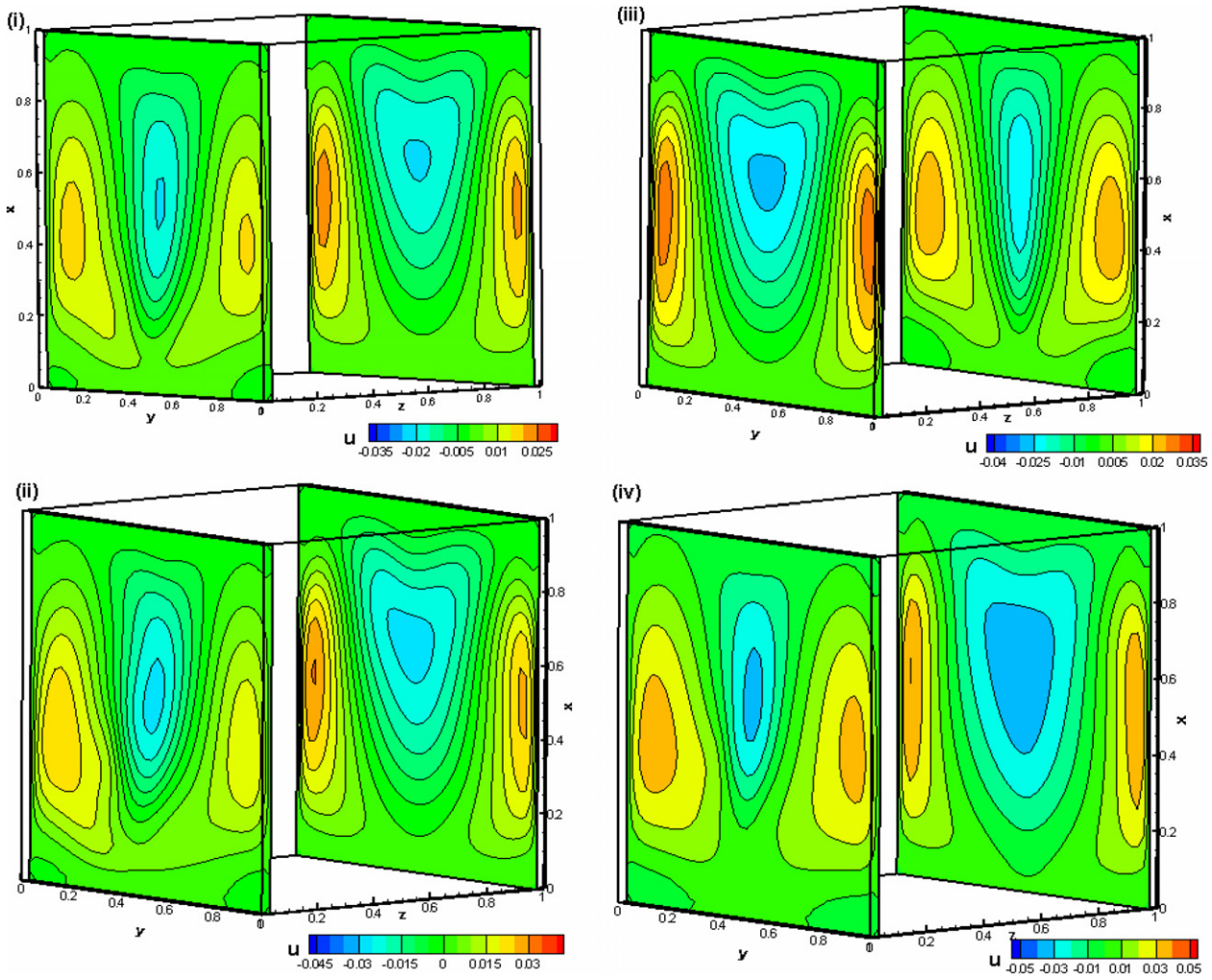

Fig. 11. Contours of the U-velocity for various Rayleigh numbers. (i) $Ra = 6730$ (steady II) (ii) $Ra = 8990$ (steady III) (iii) $Ra = 15{,}980$ (steady IV) (iv) $Ra = 15{,}990$ (steady V).

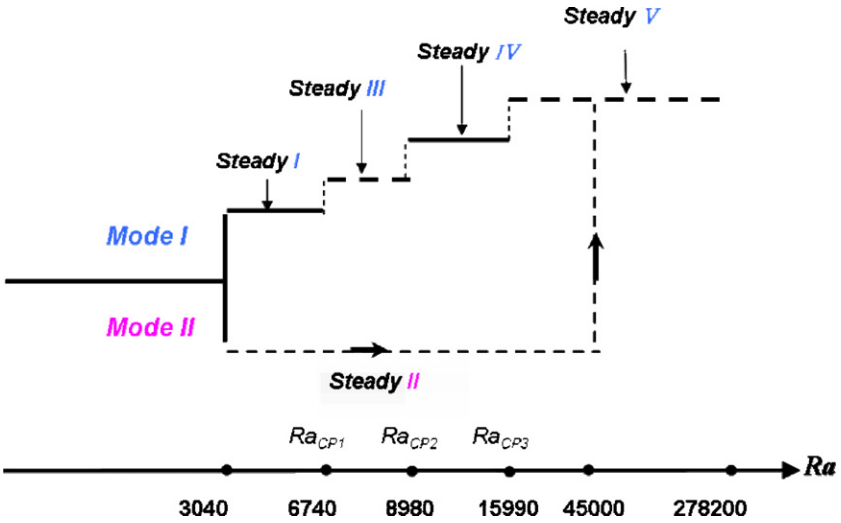

Fig. 12. Illustration of the global pitchfork bifurcation diagram based on the multiple steady-state solutions (Mode I and Mode II) at the $Y = 0.5$ plane. The solid and dashed lines denote the symmetric and asymmetric flow behaviors. Ra_{CP1}, Ra_{CP2} and Ra_{CP3} denote the occurrence of the first, second and third pitchfork bifurcations, respectively.

$Ra = 2.782 \times 10^5$ there was a transition to the periodic solutions, through which the steady convection turned into the time-dependent one, *i.e.*, periodic, quasi-periodic or chaotic motion in nature. Also the dynamic frequency-doubling bifurcation started to appear.

5. Conclusions

Laminar natural convective flow in a three-dimensional cubical cavity filled with a low Prandtl number fluid and subjected to vertical temperature gradient is numerically investigated in this study. The bottom wall and the two sidewalls up to 75% height of the cavity are hot while the top wall is cold. The two end walls and the remaining portion of the sidewalls are adiabatic. The topological theory is used to scrutinize the flow transitions and identify the critical Rayleigh numbers for transition. The numerical algorithm and the flow structures that result from its use are extensively validated. The main focus of the study is to examine the pitchfork solution bifurcation and the evolution of different symmetry-breaking orientations on the transverse and diagonal planes of the cavity as the Rayleigh number is gradually increased.

It is observed that the flow structure consisted of a pair of asymmetric counter-rotating helical cells in a double helix structure, foliated with the invariant helically symmetric surfaces containing the fibre-like fluid particle orbits. The currently investigated 3D natural convection problem is featured with the two possible symmetric conditions in geometry as well as in boundary condition. Symmetry was seen with respect to the vertical ($Y = 0.5$) and the diagonal planes. As a result, it is expected to observe the Mode I and Mode II solutions. The Mode I solution showed the symmetric nature about the Y-plane and while the other, the Mode II solution, about the diagonal plane. The flow topologies for the Mode I and Mode II were analysed by invoking the topological constraints and the structural stability criteria and were validated by the corroborative numerical evidence.

The onset of pitchfork bifurcation at $Ra = 3040$ and its evolution with respect to Ra were analysed by the L_2-error norms and the global bifurcation diagram. The Mode I solutions showed the alternate presence of the symmetric and asymmetric natures at the $Y = 0.5$ plane for the critical Ra values. Mode I solutions were, however, found to be solely asymmetric at the $Z = 0.5$ and diagonal planes. The Mode II solution was found to be asymmetric with respect to the Y, $Z = 0.5$ planes but symmetric with respect to the diagonal plane. When Ra was increased beyond 3040 there existed three critical pitchfork Rayleigh numbers, namely $Ra_{CP1} = 6740$, $Ra_{CP2} = 8970$ and $Ra_{CP3} = 15{,}990$, in which the Mode I solutions were switched from the symmetric solution to the asymmetric solution at the $Y = 0.5$ plane. At $Ra = 45{,}000$, the Mode II solutions had disappeared and there was only one asymmetric steady-state solution until $Ra = 2.782 \times 10^5$ is reached. As Ra was amplified, the transition from the 3D periodic flow to chaotic behavior showed its presence.

An unanticipated outcome of the present analysis was the discovery of solution multiplicity in the sense that the symmetric/asymmetric flow states exist over a wide range of the Rayleigh numbers. These findings suggest that multiple operating states may occur in the destabilized vertical Bridgman crystal growth process. These flow bifurcations are very interesting and the information should be useful in the design and operation of crystal growth processes.

Acknowledgement

The financial support from the National Science Council under NSC96-2221-E-002-004 and NSC96-2221-E-002-293-MY2 of Republic of China is gratefully acknowledged.

References

[1] Griffiths SK, Nilson RH, Bradshaw RW, Ting A, Bonivert WD, Hruby JM. Transport limitations in electrodeposition for LIGA microdevice fabrication. In: SPIE conference on micromachining and microfabrication process technology IV, Santa Clara: California; 1998.

[2] Brice JC. The growth of crystals from liquids. Amsterdam: North-Holland; 1973.

[3] Mcfadden B, Coriell SR. Thermosolutal convection during directional solidification. II. Flow transitions. Phys Fluid 1987;30:659.

[4] Impey MD, Riley DS, Wheeler AA, Winters KH. Bifurcation analysis of solutal convection during directional solidification. Phys Fluid A 1991;3:535.

[5] Alexander J, Amiroudine S, Ouazzani J, Rozenberger F. Analysis of the low gravity tolerance of Bridgman–Stockbarger crystal growth II. Transient and periodic accelerations. J Cryst Growth 1991;113:21.

[6] Larroude PH, Ouazzani J, Alexander JID, Bontoux P. Symmetry-breaking flow and oscillatory flows in a 2D directional solidification model. European J Mech – B/Fluid 1994;13(3):353.

[7] Bratsun DA, Zyuzgin AV, Putin GF. Non-linear dynamics and pattern formation in a vertical fluid layer heated from the side. Int J Heat Fluid Flow 2003;24:835.

[8] Lan C, Yang D. Dynamic simulation of the vertical zone-melting crystal growth. Int J Heat Mass Transfer 1998;41:4351.

[9] Lan C, Liang M. Three-dimensional simulation of vertical zone melting crystal growth: symmetry breaking to multiple states. J Cryst Growth 2000;208:327.

[10] Wille R, Fernholz H. Report on the first European mechanics colloquium on the Coanda effect. J Fluid Mech 1965;23:801.

[11] Bennacer R, Ganaoui M.El, Leonardi E. Vertical Bridgman configuration heated from below: 3D bifurcation and stability analysis. In: Third international conference on CFD in the minerals and process industries CSIRO, Australia; 2003.

[12] Davis S. Convection in a box: linear theory. J Fluid Mech 1967;30(3):465.

[13] Stork K, Muller U. Convection in a box: experiments. J Fluid Mech 1972;54(4):599.

[14] Erenburg V, Gelfgat AYu, Kit E, Bar-Yoseph PZ, Solan A. Multiple states, stability and bifurcations of natural convection in a rectangular cavity with partially heated vertical walls. J Fluid Mech 2003;492:63.

[15] Pallares J, Arroyo MP, Grau FX, Giralt F. Rayleigh–Benard convection in a cubical cavity: experimental and numerical flow topologies. Exp Fluid 2000;31(2):208.

[16] Pallares J, Grau FX, Giralt F. Flow transitions in laminar Rayleigh–Benard convection in a cubical cavity at moderate Rayleigh numbers. Int J Heat Mass Transfer 1999;2(4):753–70.
[17] Soong CY, Huang WT, Tzeng PY. A novel low-mode rigid-riding model for nonlinear dynamics analysis of a differentially heated fluid layer with and without inclination effects. Trans of the Aeronautical and Astronautical Society of the Republic of China 2005;37:77.
[18] Hunt JCR, Abel CJ, Peterka JA, Woo H. Kinematical studies of flows around free or surface mounted obstacles: applying topology to flow visualization. J Fluid Mech 1978;86:179.
[19] CFD Research Corporation (CFDRC). 216 Wynn Drive Huntsville, AL 35805: USA; 2003.
[20] MacKay RS. Transport in 3D volume-preserving flows. J Nonlinear Sci 1994;4:329.
[21] Abraham R, Marsden JE, Ratiu T. Manifolds, tensor analysis and applications. second ed. New York: Springer; 1988.
[22] Jana SC, Metcalfe F, Ottino JM. Experimental and computational studies of mixing in complex Stokes flows: the vortex mixing flow and multicellular cavity flows. J Fluid Mech 1994;269:199.
[23] Raguin G, Georgiadis JG. Kinematics of the stationary helical vortex mode in Taylor–Couette–Poiseuille Flow. J Fluid Mech 2004;516:125.
[24] Drazin PG, Reid WH. Hydrodynamic Stability. USA: Cambridge University Press; 1981.
[25] Ma T, Wang S. Structure of 2D incompressible flows with the Dirichlet boundary conditions. Discrete Contin Dyn Syst B 2001;1:29.
[26] De Vahl Davis G, Jones IP. Natural convection of air in a square cavity: a comparison exercise. Int J Numer Meth Fluid 1983;3:227.
[27] Le Quéré P. Accurate solutions to the square thermally driven cavity at high Rayleigh number. Comput Fluid 1991;20:29.
[28] Wakashima S, Saitoh TS. Benchmark solutions for natural convection in a cubic cavity using the high-order time–space method. Int J Heat Mass Trans 2004;47:853.
[29] Fusegi T, Hyun JM, Kuwahara K, Farouk B. A numerical study of three dimensional natural convection in a differentially heated cubical enclosure. Int J Heat Mass Trans 1991;34(6):1543.
[30] Janssen RJA, Henkes RAWM, Hoogendoorn CJ. Transition to time-periodicity of a natural-convection flow in a 3D differentially heated cavity. Int J Heat Mass Trans 1993;36:2927.
[31] Wan DC, Patnaik BSV, Wei GW. A new benchmark quality solution for the buoyancy-driven cavity by discrete singular convolution. Num Heat Transfer Part B 2001;40:199.
[32] Gelfgat AYu. Different modes of Rayleigh–Benard instability in two- and three-dimensional rectangular enclosures. J Comput Phys 1999;156:300.
[33] Puigjaner D, Herrero J, Giralt F, Simó C. Stability analysis of the flow in a cubical cavity heated from below. Phys Fluid 2004;16:3639.
[34] Robinson SK. Coherent motions in the turbulent boundary layer. Ann Rev Fluid Mech 1991;23:601.
[35] Chiang TP, Tony WHS, Tsai SF. Topological flow structures in backward-facing step channels. Comput Fluid 1997;26:321.
[36] CFD Analyser Tecplot 10.0-4-10, Tecplot Inc, USA.
[37] Ganaoui MEL, Bontoux P. An homogenisation method for solid–liquid phase change during directional solidification. In: Nelson RA, Chopin T, Thynell ST, editors. Numerical and Experimental Methods in Heat Transfer. ASME H.T.D., 1998;361(5):453.
[38] Feigenbaum M. Quantitative universality for a class of nonlinear transformations. J Stat Phys 1978;19:25.
[39] Sonda P, Yeckel A, Daoutidis P, Derby JJ. Improved radial segregation via the destabilizing vertical Bridgman configuration. J Cryst Growth 2003;260:263.
[40] Sonda P, Yeckel A, Daoutidis P, Derby JJ. Hopf bifurcation and solution multiplicity in a model for destabilized Bridgman crystal growth. Chemical Eng Sci 2005;60:1323.